Materials Science & Engineering A 872 (2023) 144222

Contents lists available at ScienceDirect

Materials Science & Engineering A

journal homepage: www.elsevier.com/locate/msea

Local mechanical properties and precipitation inhomogeneity in large-grained Al–Mg–Si alloy

Anette B. Hagen [a,*], Sigurd Wenner [a], Ruben Bjørge [a], Di Wan [c], Calin D. Marioara [a], Randi Holmestad [b], Inga G. Ringdalen [a]

[a] Department of Materials and Nanotechnology, SINTEF Industry, P.O. Box 4760 Torgarden, NO-7465 Trondheim, Norway
[b] Department of Physics, Norwegian University of Science and Technology (NTNU), NO-7491 Trondheim, Norway
[c] Department of Mechanical and Industrial Engineering, NTNU, NO-7491 Trondheim, Norway

ARTICLE INFO

Keywords:
Precipitate strengthening
Aluminium alloys
Nanoindentation
TEM

ABSTRACT

Al–Mg–Si (6xxx series) alloys show excellent mechanical properties due to the precipitates formed during heat treatment. However, heat treatment of these alloys results in a soft precipitation free zone (PFZ) close to grain boundaries that weakens them and promotes fracture, and thereby reduces the ductility of the material. This study provides quantitative insights into the mechanical properties and underlying plasticity behavior of Al–Mg–Si (6xxx series) alloys through combined nanoindentation hardness measurements and in-depth characterization of the microstructure adjacent to the PFZ region and in the grain interior. Experimental nanoindentation, transmission microscopy (TEM) and electron channeling contrast imaging results confirm the weakening effect from PFZ by means of a reduced hardness close to grain boundaries. The nanoindentation hardness mapping also revealed an increase in hardness a few micrometers from the grain boundary with respect to the grain interior. Precipitate quantification from TEM images confirms that the hardness increase is caused by a locally higher density of precipitates. To the authors' best knowledge, this harder zone has not been recognized nor discussed in previously reported findings. The phenomenon has important implications for the mechanical properties of large-grained (> 100 μm) aluminium alloys.

1. Introduction

Aluminium is one of the most utilized materials in the automotive industry. The increasing demand for fuel-efficient vehicles to reduce energy consumption and air pollution has also increased the demand for aluminium. The 6xxx series aluminium alloys (Al–Mg–Si) form one of the main groups of age hardenable alloys and are widely used in applications such as transportation and construction due to low weight, high strength and good formability. 6xxx series aluminium alloys are commonly used in car safety components such as crash boxes and bumper systems. Decreasing the weight while also retaining energy absorbing capabilities is important when optimizing the heat treatment and work hardening of these materials. The most important strengthening mechanism in 6xxx alloys is dislocation pinning by coherent precipitates formed during artificial aging. Precipitation in these alloys has therefore been investigated in nanoscale [1–5]. The initial stage of the precipitation process involves formation of atomic clusters and Guinier–Preston (GP) zones from supersaturated solid solution (SSSS). Subsequently, β'' precipitates form as coherent needles in the (001) Al crystallographic directions, typically giving Al–Mg–Si alloys their maximum strength [6]. The β'' needles eventually transform into semi-coherent β' rods or other over-aging phases, which ultimately, transform into β-Mg_2Si platelets [6], and represent the true equilibrium phase. This precipitation sequence can be summarized as follows

$$SSSS \rightarrow \text{solute clusters} \rightarrow \text{GP zones} \rightarrow \beta'' \rightarrow \beta', (\text{U1,U2,B}') \rightarrow \beta, \text{Si} \quad (1)$$

Precipitation usually occurs homogeneously throughout the aluminium grains, with some exceptions. Precipitate free zones (PFZ) form along grain boundaries (GBs) during the heat treatment of aluminium alloys and consist of a region without strengthening precipitates. The PFZs are soft zones in which plastic strain tends to localize and contribute to both the initiation and propagation of damage and fracture. How and where strain localization occurs in the PFZ is an important question, as this is often a limiting factor for the ductility of the material [7]. One of the main mechanisms for formation of PFZs is diffusion of vacancies towards the GB [8]. This creates a zone depleted of vacancies, which are required for substitutional diffusion and therefore nucleation and growth of precipitates. Another factor in the

* Corresponding author.
E-mail addresses: anette.brocks.hagen@sintef.no (A.B. Hagen), inga.g.ringdalen@sintef.no (I.G. Ringdalen).

https://doi.org/10.1016/j.msea.2022.144222
Received 7 September 2022; Received in revised form 18 October 2022; Accepted 22 October 2022
Available online 28 October 2022

formation of PFZs along GBs is the fact that GBs themselves can be potential nucleation sites for precipitates, causing diffusion of solutes towards the GBs. Precipitates will be formed at the GBs early during the heat treatment. The growth of these precipitates is thereafter draining the region near the GB for solute atoms, making later nucleation of precipitates in the region near the GB impossible. A third factor influencing the formation of precipitates is that as the precipitates grow in length, some will eventually reach the GB (GB) and are expected to dissolve quickly. Thus, a PFZ width similar to the average precipitate length is expected in all cases.

Several studies have investigated the extent of the PFZ and its influence on deformation and mechanical properties [9,10]. Dislocations interact with precipitates in a manner that strongly depends on the amount of deformation. Dislocation pile-ups are frequently observed along the interface between the grain interior and the PFZ. In heavily deformed areas, a dense wall of dislocations along the interface can separate the PFZ from the adjacent grains and form a band-like structure with slightly different crystallographic orientations than the grain interior [10]. In addition to the band-like structure, the PFZ can also be partitioned in smaller grains in the size range of the PFZ width. However, the PFZ consisting of smaller grains are more frequent at larger strains. This indicates that the different characteristics observed in the PFZs, depend on the strain localization during deformation and orientation of the loading axis relative to the crystal orientation and GB planes. Consequently, the different PFZs affect the work hardening and subsequently the fracture initiation in aluminium alloys during deformation [10].

By manipulating the thermo-mechanical processing of age hardenable aluminium alloys, the crystallographic texture and precipitate structure can be controlled to obtain the desired mechanical properties. Slow cooling rates – i.e. air-cooling – after solution heat-treatment Al–Mg–Si alloys are shown to influence the precipitate morphology and result in a wider PFZ than after water-quenching. The yield strength of Al alloys can be significantly reduced by air cooling, particularly in high solute alloys [11].

The macroscopic mechanical properties of Al alloys can easily be obtained from conventional testing methods. However, material failure of any bulk material starts with the local formation and accumulation of defects at the micro-scale, finally leading to fracture by an advancing crack. Therefore, testing at the nano- and micrometer length scale is necessary to obtain an in-depth understanding of the interplay between plastic deformation and microstructural features such as GBs, PFZ's and precipitates. The PFZs are usually within the size range from ten to hundreds of nanometers. Nanoindentation is currently the only nanomechanical testing method able to determine the accurate hardness distribution at and close to the PFZ. Abundant investigations using nanoindentations are available for various materials. However, the mechanical properties of the PFZ and the resulting effect on strain localization, ductility and fracture of 6xxx series aluminium alloys are not yet fully understood.

Ogura et al. [12] performed nanoindentation on Al–Zn–Mg alloys and revealed that nanohardness across the GBs with PFZs could be divided into three hardness regions, where nanohardness decreased with decreasing distance to the GB. The obtained hardness was influenced by the solute concentration and precipitate distribution. A decrease in nanohardness with decreasing distance from the GB was also observed in Al–Cu–Si–Ge alloys by Radmilovic et al. [13]. Also here, three different regions adjacent to the GB were defined and correlated to the different diffusivity of Cu, Si and Ge and vacancies. Hashimoto et al. [14,15] suggested from combined nanoindentation and TEM investigations that the GB misorientation could influence the aging precipitation and the mechanical properties close to GBs and PFZs in Al–Mg–Si alloys.

In this work, we aim to expand the knowledge of the mechanical properties of the near-GB regions in Al–Mg–Si alloys by investigating the change in hardness across the GB and PFZ with increasing distance to the GB. Further, we correlate plasticity and dislocation behavior with the precipitation and solute distribution in the microstructure, through combined nanoindentation, transmission electron microscopy (TEM) and electron channeling contrast imaging (ECCI).

2. Methodology

2.1. Alloy composition and processing

The experiments were performed using a rolled Al–Mg–Si alloy with composition similar to AA6060: 0.46 wt% Mg, 0.54 wt% Si. The alloy is nearly free of Fe and Mn (3.4 ppm Fe and 0.3 ppm Mn) such that no large primary particles or dispersoids are formed. The low content of Mg and Si also decreases the amount of stable phases precipitated on the grain boundaries. This ensures large grains and therefore long segments of uninterrupted GBs with no influence from particles other than nm-sized precipitates. The alloy was homogenized for 535 °C for 24 h, then rolled to a thickness of 3 mm. Due to the absence of grain refining particles (e.g. TiB_2), the alloy is completely recrystallized and contains mainly large grains (> 100 μm) and high-angle GBs.

Solution heat treatment was done at 540 °C for 15 min, followed by passive cooling in still air (kept at room temperature for 20 min). Artificial aging was done at 185 °C for 5 h. This is a typical heat treatment used to bring AA6060 alloys to peak hardness, a so-called T6 heat treatment. Two additional samples were prepared and tested: a precipitate free reference material with T4 heat treatment – which is the same as T6 but without artificial aging – and a T6 sample that was water quenched instead of air cooled. The three different conditions will be referred to as T6AC, T4AC and T6WQ.

The samples were ground and polished in the rolling normal plane, ending with a nap cloth with 1 μm diamond suspension. Finally the surface was electropolished for 10 s with a Struers Polectrol at 20 V using the Struers A2 electrolyte. This creates a smooth surface with minor topographical changes near GBs, which is ideal for pinpointing the GB locations during nanoindentation experiments. The surface is also of good quality for electron microscopy analysis including electron back-scatter diffraction (EBSD).

2.2. Orientation mapping

EBSD maps were acquired with a Hitachi SU6600 scanning electron microscope (SEM), using a Nordif fluorescent screen detector. The data was analysed using the MATLAB™ toolbox MTEX to find GB misorientations for selecting GB's for nanoindentation, and grain orientations for ensuring that ⟨001⟩ Al zone axes were available during TEM preparation. The investigated areas in T6AC are shown in the SEM micrograph with corresponding EBSD analysis in Fig. 1.

2.3. Nanoindentation

Nanoindentation was performed using a Hysitron TI 950 TriboIndenter system with a scanning probe microscope (SPM) imaging option. Nanohardness measurements were conducted on all three samples, i.e. T6AC, T6WQ and T4AC. SPM imaging was used to accurately locate the GBs and PFZ areas, where the nanoindentations were performed. The indentations were performed diagonally across the GB and PFZs using a peak load of 1500 μN with the standard three-sided Berkovich tip (half angle of 65.35°). A total of 350 nanohardness measurements were performed in the regions of interest, i.e., grain boundary 1 (GB1), grain boundary 2 (GB2) and grain boundary 3 (GB3) in T6AC, shown in Fig. 1. Additionally, indentations were performed in the center of the grain, in order to obtain the intrinsic mechanical properties of the grains without any influence from possible plasticity interaction with the GBs. also 50 and 70 indentations were performed across one GB in T4AC and T6WQ, respectively.

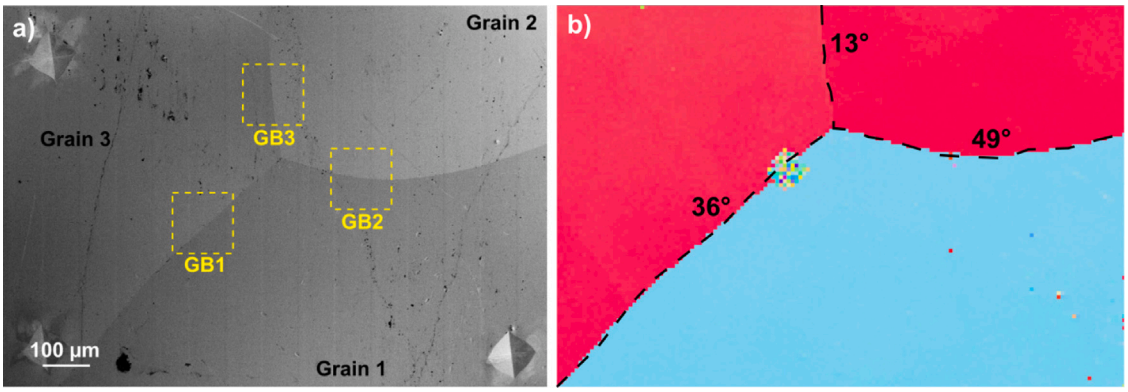

Fig. 1. T6AC testing areas. (a) SEM image and (b) EBSD map analysis with the corresponding GB misorientations given. The red grains have surface normals close to ⟨001⟩ while the blue grain has surface normal close to ⟨111⟩. (For interpretation of the references to color in this figure legend, the reader is referred to the web version of this article.)

Prior to testing, an area function calibration was performed to eliminate non-ideal shape effects of the tip. The nanohardness was calculated using the conventional Oliver and Pharr method [16]. Additional nanoindentations were performed at a lower peak load (300 μN) to minimize the plasticity below the indenter and with various distances between the indents, i.e. 2, 3 or 6 μm, to ensure the reliability of the results.

2.4. Electron channeling contrast imaging (ECCI)

ECCI was conducted in a Quanta 650 field-emission gun scanning electron microscope (FEG-SEM, ThermoFisher Inc.). The SEM was operated at 30 kV accelerating voltage with an aperture of 30 μm. A four-quadrant solid-state backscattered electron (BSE) detector was used to collect the signal. During imaging, the specimen was tilted by up to 3° to meet the dual-beam diffraction condition in order to obtain the optimum channeling contrast. With the channeling effect, the observed contrast is very sensitive to local misorientations, which imply deformations and the presence of dislocations. A comprehensive theoretical background of this technique can be found in elsewhere [17].

2.5. TEM - Plan view and precipitate quantification

A plan view (surface-parallel) slice through an indentation grid at GB1 (T6AC) was made for scanning precession electron diffraction (SPED) measurements of local misorientations. All preparation was done with the focused ion beam (FIB) lift-out method, using a FEI Helios G4 FIB/SEM instrument. The specimen was prepared as follows: An array of indentations was covered by layers of electron-deposited platinum and ion-deposited carbon. The volume containing the indentations was milled out using 30 kV Ga^+ ions. The volume was lifted out, rotated and attached to a Cu TEM half-grid, maintaining the original surface plane normal as the TEM viewing direction. The sample was thinned, removing the deposited platinum while retaining a < 100 nm thick indented near-surface region around a few indents. The final thinning steps were done with 2 kV Ga^+ ions.

SPED investigations were done using a JEOL JEM-2100F microscope with a NanoMegas SPED system. The acceleration voltage was 200 kV. The spot size in SPED was 10 nm, and the convergence angle was 1.0 mrad. The beam was processed 0.5° at 100 Hz. An externally mounted optical Stingray camera captured diffraction patterns on the fluorescent screen, with a 40 ms exposure time per pixel.

The diffraction patterns were indexed in the NanoMegas Index software and further processed in MTEX. A half-quadratic minimization filter was used to denoise the orientation data. The first-order kernel average misorientation was computed by averaging the orientation difference between each pixel and its four nearest neighbors. A threshold of 2 degrees was used to eliminate outliers.

Cross-sectional TEM samples for precipitate quantification were extracted from T6AC using the FIB lift-out method from two locations: an area including GB3 and 100 μm away from GB3, inside grain 2. Precipitate dimensions and distribution 2 ± 1 μm from GB3 and in the grain interior were quantified following the established methodologies for Al alloys [18]. Precipitate needle lengths and cross-section areas were measured from bright-field TEM images, while precipitate number density was determined from dark-field TEM images. The sample thickness was measured using two-beam convergent beam electron diffraction [19].

2.6. Chemical mapping

To investigate the variation in solute content around GBs, STEM-EDS maps comprising GBs and PFZs were acquired from the T6AC and T4AC conditions. A JEOL JEM-2100F microscope with an Oxford X-MAX 80 EDS detector was used for this purpose. In this case the samples were prepared by mechanical polishing and electropolishing. A Struers TenuPol-5 was used, with a voltage of 20 V and an electrolyte consisting of 1/3 nitric acid and 2/3 methanol, cooled to −30 °C.

To obtain a more accurate and quantitative element measurement at higher scales, electron probe microanalysis (EPMA) using both 30 μm line scans and point analysis was performed across three GBs and in the grain interior with a step size of 1 μm. Measurements were performed using a JXA-8500F JEOL instrument equipped with a wavelength dispersive X-ray spectrometer (WDS) and an energy dispersive X-ray spectrometer (EDS).

3. Results

3.1. Nanohardness

Fig. 2(a) and (b) show the hardness profile obtained from T6AC across GB2 and GB3, respectively. The average nanohardness representative for the grain interior in the tested grains is approximately 1.1 GPa, indicated by dotted lines. Nanoindentations were performed across GB1 (misorientation 36°), GB2 (49°) and GB3 (13°) in T6AC, with an indent spacing of 2, 3 and 6 μm, shown in Fig. 3(a), (b) and (c), respectively. For comparison, nanoindentation hardness profiles were also obtained from T6WQ and T4AC, presented in Fig. 4.

Overall, the hardness profiles across all three GBs in T6AC show comparable characteristics, with increasing hardness as they approach the PFZ, followed by a sharp decrease at the PFZ. The hardness can be divided into the following regions; (I) PFZ, (II) the transition region (defined from [12]), (III) the near-GB region, consisting of the hardness peak and transition to (IV) the grain interior, where hardness approaches a constant value representing the intrinsic properties of the grain, highlighted in Fig. 5 with data from GB3. The hardness

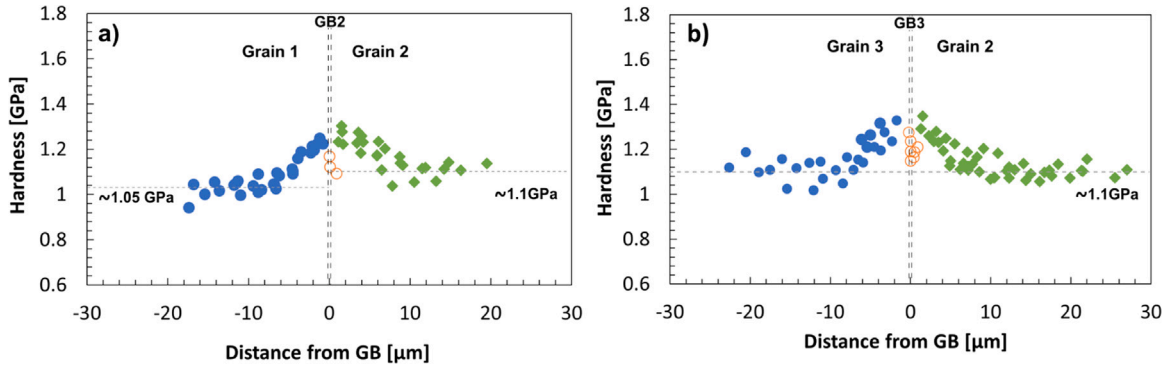

Fig. 2. Nanohardness profiles from all tests performed across (a) GB2 and (b) GB3 in T6AC. The average hardness from each grain interior are indicated with a dotted line. The indent spacing was 6 µm.

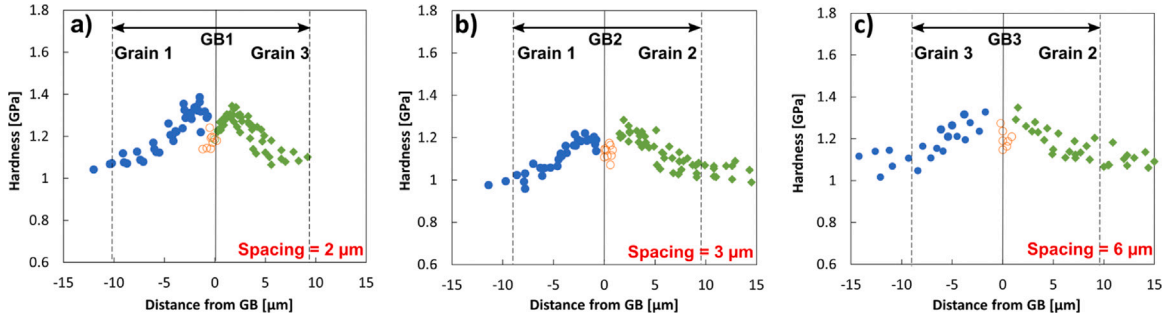

Fig. 3. Nanohardness profiles from (a) GB1, (b) GB2 and (b) GB3 in T6AC with indent spacings of 2, 3 and 6 µm, respectively.

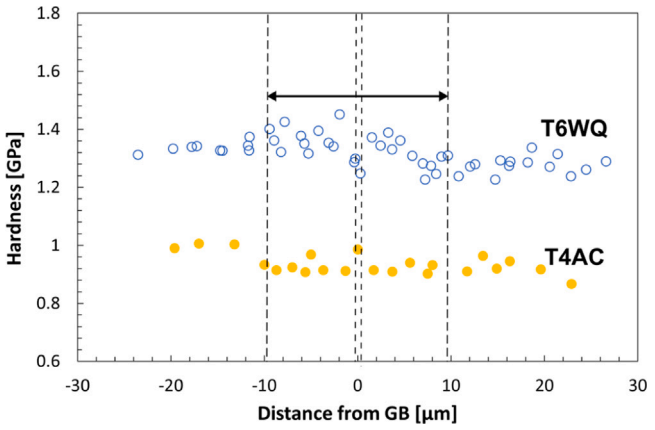

Fig. 4. Nanohardness profiles obtained from T4AC and T6WQ. Distance between indents was 6 µm. The dotted lines indicate the area with elevated hardness in T6AC.

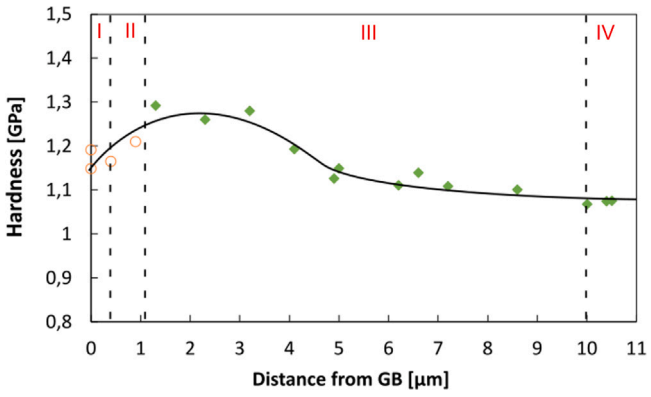

Fig. 5. Nanohardness profile obtained from one of the nanoindentations grids conducted across GB3 in T6AC. The hardness profile is divided into four regions; I: the PFZ, II: the transition area, III: high density precipitate distribution and IV: grain interior.

peak, detected in region (III), occurs about ~2–3 µm from the GB and gradually decreases to hardness values representative for the grain interior, about ~10 µm from GB, depending on the crystallographic orientations of each grain and the GB rotation.

The hardness profile obtained for T4AC, differs from that observed in T6AC and T6WQ, as shown in Fig. 4. The hardness in T4AC is constant towards and across the GB. The T6WQ on the other hand, shows a hardness increase about 8–10 µm from the GB (highlighted with the dotted lines), comparable to that observed for T6AC.

3.2. Electron channeling contrast imaging (ECCI)

Fig. 6 shows the ECC images focusing on GBs in T6AC and T4AC before nanoindentation. The precipitation free area close to the GB is confirmed for the T4AC specimen. Only statistically stored dislocations were found close to the GB. For the T6AC specimen, precipitates can be clearly detected as bright features in the grain matrix. A PFZ of roughly 200 nm can be measured across the GB (Fig. 6b). Fig. 7 shows the ECCI investigation on the indents adjacent to the GB1 in T6AC. Clear plastic deformation zones on the specimen surface can be seen in the vicinity of the triangular shaped Berkovich indents. When the indents are far away from the GB, the plastic zones have similar shapes for all indents. However, when the indent meets the GB, the shape of

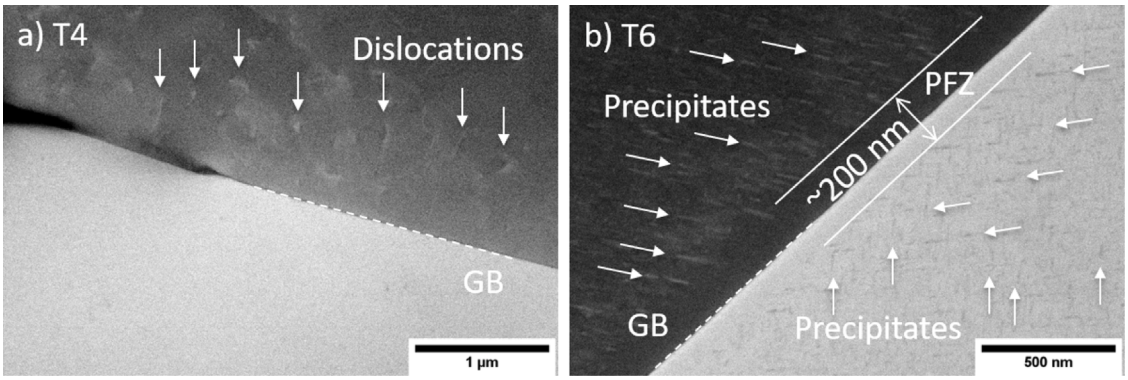

Fig. 6. ECC images focusing on GB from (a) T4AC and (b) T6AC specimens. The dashed lines indicate the GB. The arrows in (a) indicate dislocations. The arrows in (b) indicate the precipitates close to the GB. A PFZ with a width of 200 nm close to the GB can be noted in the T6 specimen.

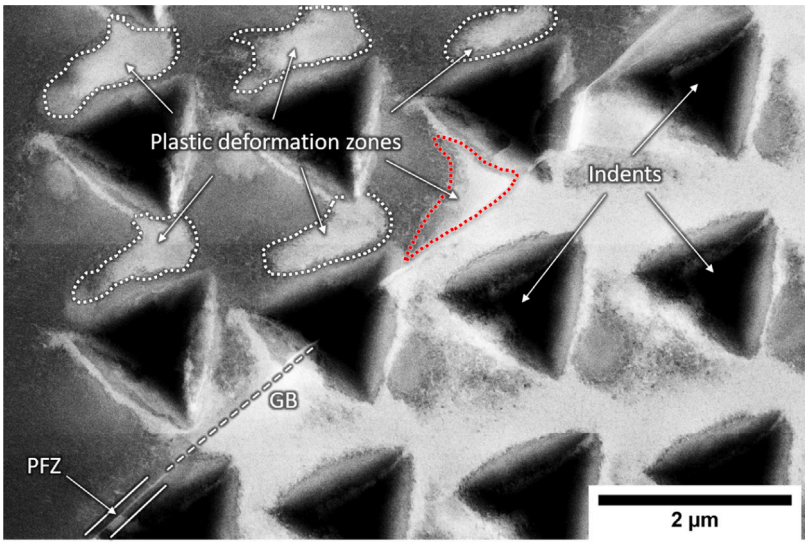

Fig. 7. ECC image showing the Berkovich indents across GB1 in T6AC. The contrasts in the image indicate plastic deformation depending on the lattice orientation. (For interpretation of the references to color in this figure legend, the reader is referred to the web version of this article.)

the plastic deformation zone is significantly distorted and elongated along the GB (see the region highlighted by the red dotted line in Fig. 7). This gives a clear indication that the GB is interfering with the plastic deformation during nanoindentation close to GB. The PFZ as determined from images with higher magnification (i.e. Fig. 6b) is also marked in Fig. 7 for reference.

3.3. TEM/SPED

The TEM sample preparation was conducted as described in Section 2.5 on a 4 × 12 nanoindentation array across GB1 in T6AC, shown in Fig. 8(a). Fig. 8(b) shows a bright-field TEM image of the highlighted area from (a), focusing on the four nanoindents close to the GB. Dark bands (bending contours) show, in a manner similar to ECCI, the areas with changes in the lattice orientation, and therefore the diffraction conditions. Fig. 8(c) shows a bright-field TEM image from an area away from the nanoindents, with the upper grain oriented exactly along the [001] zone axis. Needle-shaped β'' precipitates are observed, all oriented in the ⟨100⟩ Al lattice directions. The PFZ around the GB is measured to 220 nm on the upper side, giving an approximate full PFZ width of 440 nm around this GB. Note that this is smaller than the indents, and much smaller than the plastic zones of the indents.

In Fig. 9, the results of the SPED analysis of T6AC (GB1) is presented. The square highlighted in 8(b), shows the investigated SPED area. The two scans were acquired with different sample tilt: The first (a,c) with the electron beam along the original surface normal (each grain being 10–15° off-zone), and the second (b,d) with the electron beam along [001] in the upper grain. Different features are easier to observe/measure in each of the conditions. In particular, short-range orientation differences appear sharper in the zone-axis condition.

The kernel average misorientation highlights areas with short-range orientation changes. The blue circle in Fig. 9(c) marks the strain field in-between the indentations, also observed with ECCI. The misorientations across such areas are typically 1°. A more abrupt orientation change is seen around indent 1, where tiny pockets of 2–3° misorientation are formed between the indentation and the GB (blue arrows in Fig. 9(d). The misorientation is high enough to classify the pockets as subgrains, separated from the upper grain by geometrically necessary dislocations [10].

3.4. Precipitate quantification

Dark-field TEM images of the precipitate microstructures in the two investigated regions, 2 µm and 100 µm from GB3, are shown in Fig. 10. The average precipitate measurements are given in Table 1. The microstructure near the GB comprised a significantly higher number density and length of precipitates than the microstructure in the grain interior, which also results in a higher precipitate volume fraction of precipitates.

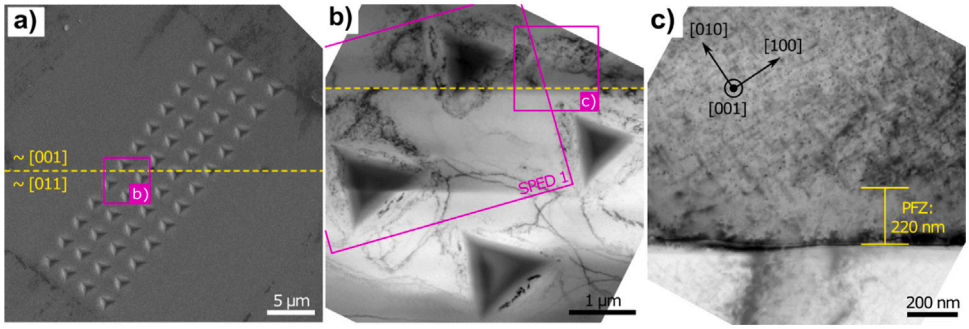

Fig. 8. TEM overview of a 4 × 12 nanoindentation array around GB1 in T6AC. (a) SEM image of the array. (b) Bright-field TEM image of four indents close to GB1. (c) Bright-field image of precipitate microstructure close to GB1, in a [001] orientation.

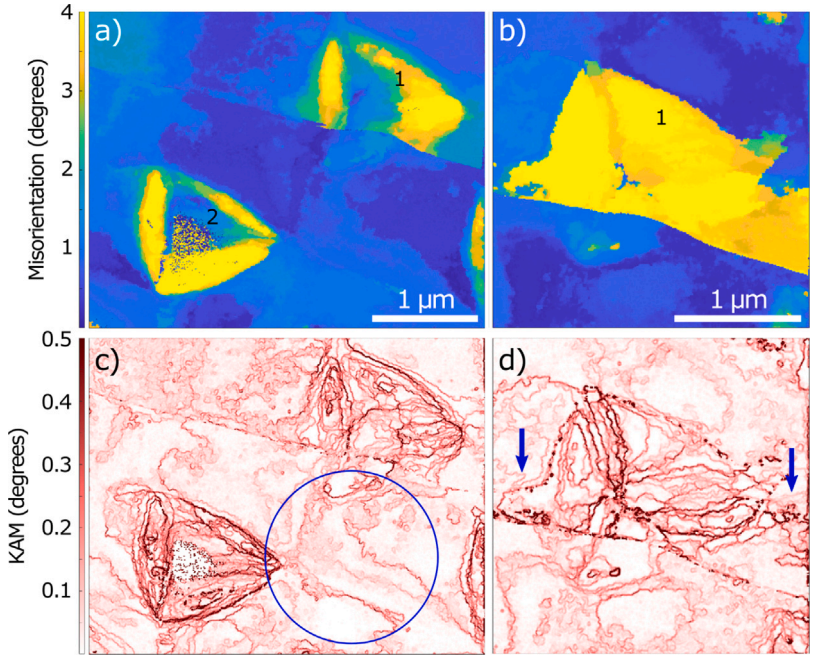

Fig. 9. Results from SPED analysis of T6AC. (a,c) Map with two indentations close to GB1. (b,d) Map from indentation 1, in a [001] orientation. (a–b) Angle of misorientation from the average value in each grain. (c–d) Kernel average misorientation. The blue circle highlight strain fields in-between indentations and the blue arrows point towards abrupt orientation changes between indentation and GB.

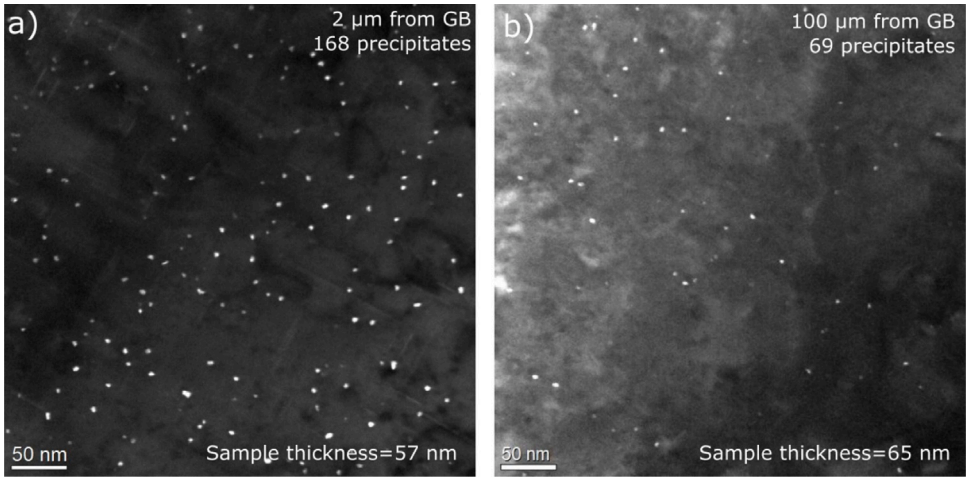

Fig. 10. Dark-field TEM image of precipitate microstructure in T6AC (a) 2 µm and (b) 100 µm from the GB3, in the [001] Al zone axis orientation.

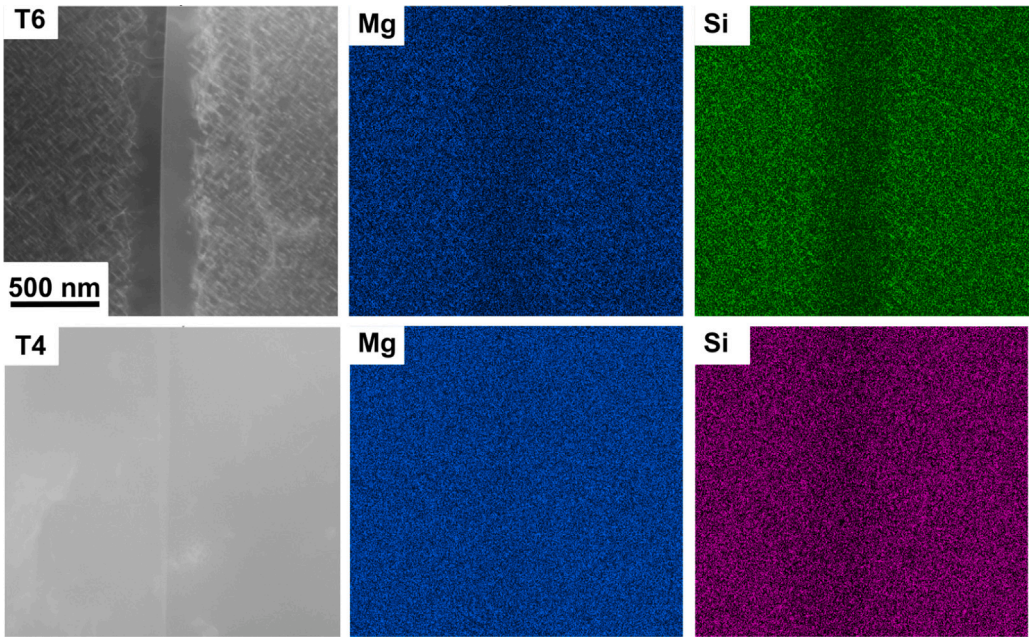

Fig. 11. Annular dark-field STEM image and EDS maps of the Mg and Si content across the GB and PFZ in the T6AC.

Table 1
Average precipitate measurements from two different regions within grain 2 in T6AC.

	2 μm from GB3	Grain interior
Number density [μm^{-3}]	34 600 ± 2100	24 200 ± 1300
Avg. precipitate length [nm]	51 ± 3	29 ± 1
Avg. cross section [nm^2]	11 ± 0.7	11 ± 0.6
Volume fraction [%]	2.0 ± 0.2	0.80 ± 0.1

3.5. EDS and EPMA

Fig. 11 shows the STEM-EDS map across GBs in the T6AC and T4AC conditions. In T6AC, the precipitates are visible both in the STEM image and the elemental Mg and Si maps. There is a zone depleted of Mg and Si close to the GB and about 400 nm in width. This corresponds to the PFZ as seen in the STEM image. The T4AC condition also has a solute depleted zone around the GB, but this is much less significant than in T6AC.

Fig. 12 represents the average EPMA line scans of Si and Mg across 3 different GBs in both T6AC and T4AC. The Si and Mg content in T4AC seems to be constant across the GBs with an average content of 0.61 wt% for both elements. The Si and Mg content in T6AC are averaged to 0.51 and 0.53 wt% for Si and Mg, respectively. However, the Mg content is slightly higher closer to the GB compared to that of Si. The Mg content was determined to be 0.54 wt% at 5 μm from the PFZ towards the grain interior, compared to 0.51 wt% for Si.

4. Discussion

4.1. Nanohardness and microstructure

The hardness profiles obtained from nanoindentation across GB1, GB2 and GB3 in T6 (both air cooled and water quenched) (Fig. 3) are consistent with previous literature which reports the hardness to be reduced close to GBs in Al–Mg–Si alloys [12,14,15]. This has been correlated to local variations in solute concentration and precipitate distribution. Ogura et al. [12] reported a significant drop in solute concentration and nanohardness with decreasing distance to the GB for an Al–Zn–Mg based alloy. Similar findings were confirmed in a peak aged Al–Mg–Si alloy, in a recent work by Hashimoto et al. [14,15]. The reduced nanohardness obtained from the transition area and towards the GB, were correlated to the diffusion of solute towards the GB, which again results in the formation of a PFZ and subsequently, a low concentration region where precipitates were coarsely distributed due to less available solutes for precipitation.

The above descriptions are in line with the exhibited hardness trend in the vicinity of the GBs in the T6AC specimens. TEM and ECCI results shown in Figs. 6 and 8 confirm a full PFZ width in the range of 200–440 nm, giving rise to the local hardness variations across the GB. Interestingly, the results reveal a distinct hardness peak 2–3 μm from the GB, elucidated in Fig. 5. The discernible trend in T6 is captured for all nanoindentation arrays located across a GB in T6AC and T6WQ. Precipitate statistics obtained from TEM samples extracted 2 and 100 μm from GB, clearly reveals a significantly higher density of precipitates 2–3 μm from the GB where the hardness peak occurs, Fig. 10. Load–displacement curves shown in Fig. 13 clearly reflect increased hardening for indentations performed here.

To the authors‘ knowledge, such a harder zone close to a GB has not been recognized nor discussed in previous reported findings. In previous nanoindentation studies with the purpose to study the hardness in the PFZ and the “Transition zone” [12,14,15], indents up to 8 μm away from the GB are included. Therefore, the investigated hardness profile is limited to a relatively narrow zone. In contrast, the current study performed nanoindentations up to 30 μm from the GB. However, from the plots in the work by Hashimoto [14], a tendency of hardness reduction can be observed about 8 μm from the GB, which is consistent with the findings in this work.

Fig. 5 shows the hardness profile obtained from a test grid of 7 x indents across GB3 in T6AC. Based on TEM observations in this work and the findings from previous nanoindentation studies on Al–Mg–Si alloys in peak aged condition [12,14,15], the hardness profile across the GB can be divided into the following regions: (I) PFZ, (II) the transition region, (III) precipitation hardening and (IV) grain interior. Possible strengthening mechanisms in this alloy includes solid solution hardening, GB strengthening and precipitation hardening [13]. β'' is the most common precipitate phase existing in the peak hardened state and precipitation strengthening is considered to be the main strengthening mechanism in these alloys [20]. The statistical assessment of the precipitates presented in Table 1, shows that number density of

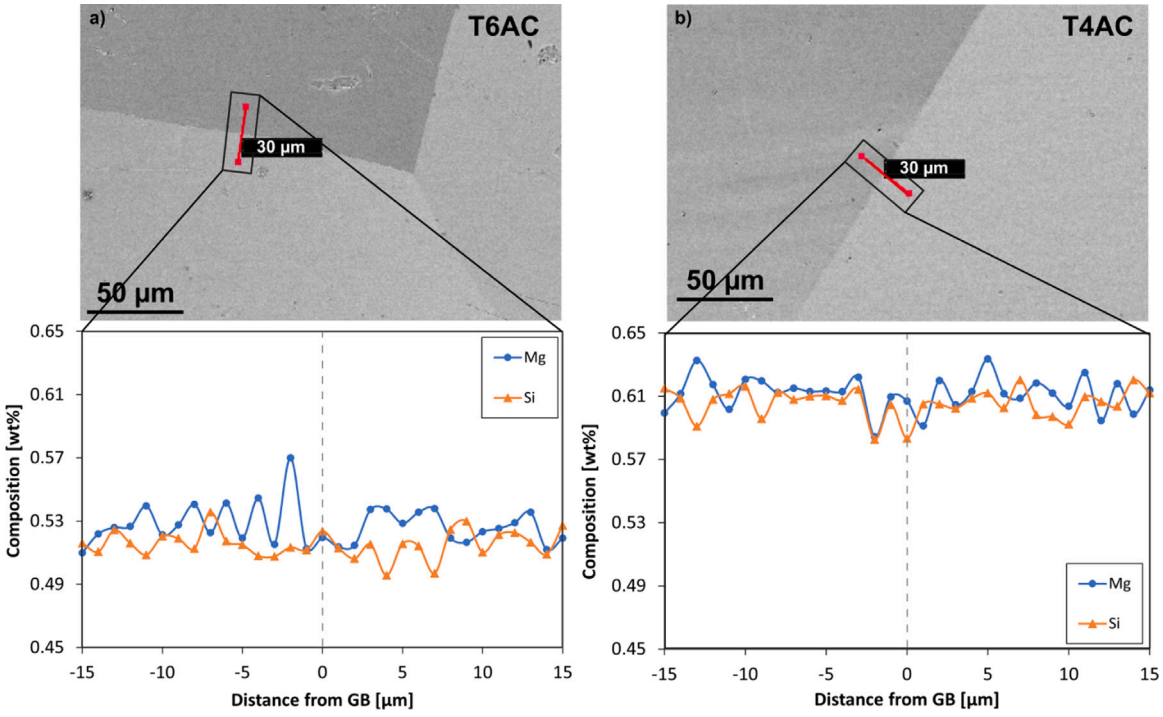

Fig. 12. EPMA line scans across GBs in (a) T6AC and (b) T4AC with one scan location highlighted in the SEM images. The plot is averaged from three scans from various locations across similar GBs.

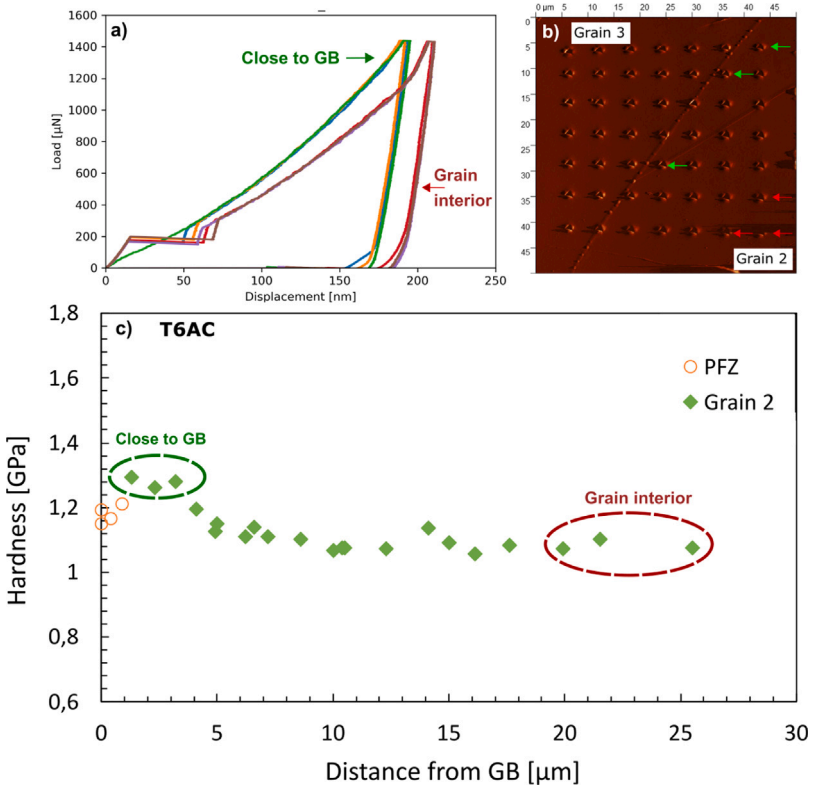

Fig. 13. (a) Representative load–displacement curves from nanoindentations in T6AC near the GB3 in and in the grain interior with the corresponding (b) SPM image of the indentation grid and (c) the hardness profile from GB3 and towards the grain interior.

precipitates increases from 24 200 to 34 600 μm^{-3} in the near-GB-area compared to that found 100 μm from the GB. The hardness increase in region III can be rationalized with a higher density and length of β'' precipitates within this region, since this provides more points where dislocations are pinned per volume.

From Figs. 8 and 10, it is confirmed that needle shaped β'' precipitates exists in the ⟨001⟩ Al lattice direction just outside the PFZ and in the grain interior. During aging, the Mg–Si clusters and the GP-zones transform into β'' [6]. However, the distribution and/or morphology of the precipitates can vary depending of the solute concentration of Mg and Si in the matrix and the concentration of vacancies. Solid solution strengthening influences the hardness depending on the concentration of Mg and Si in solid solution.

The results from EPMA show a higher Mg and lower Si concentration a few micrometers from the GB, compared to that measured 10–15 μm from the GB (Fig. 12), indicating different solute levels in the two regions. In general, the PFZ is depleted of vacancies and no precipitates can form. It is possible that longer-range diffusion kinetics has left a slightly Mg-enriched zone in a few μm outside the PFZ. However, it is speculated if there might be a long-range weaker partial depletion that generates the findings in "regions III". Recent findings in Al–Mg–Si alloys suggest a higher diffusivity of Si towards the GB than for Mg [21]. Consequently, a higher depletion of Si adjacent to the GB could be expected, resulting in the lower concentration close to PFZs which was confirmed by the EPMA analyses. Mg-rich alloy compositions are known to generate a lower number density of precipitates compared to Si-rich compositions, which results in a lower hardness [22]. However, the differences in Mg and Si concentration are very small and might not be sufficient to conclude on the reason for a higher density of precipitates in region III.

Another possibility is an effect of inhomogeneous vacancy concentration. Quenched-in vacancies from solution heat treatment (SHT) are generally accepted to play an important role during diffusion and nucleation of hardening precipitates. However, recent studies indicate that the vacancy diffusion is quick enough for the concentration to decreases to an equilibrium level during seconds at artificial aging temperatures [23]. This means that equilibrium vacancies have to be used for precipitation. Further, it is known that the β'' phase consumes vacancies to grow laterally [1]. Therefore, it is possible that the precipitation process itself depletes vacancies locally. To maintain an equilibrium concentration, fresh vacancies must enter the grains through GBs or from dislocation-based vacancy sources [24]. For materials with large grains, as in the current study, the combination of vacancy diffusion and depletion by growing precipitates could therefore limit the amount of vacancies that reaches the middle of the grains. If this occurs, it would create a zone with a more developed precipitate microstructure close to GBs than in the grain interiors. Additional experimental work and chemical analysis are needed to explain inhomogeneities in precipitate distribution in the vicinity of the GB.

4.2. Dislocation–grain boundary interaction

Fig. 7 shows an ECC image of the Berkovich indentation performed near GB1 in T6AC with an indent spacing of 2 μm. The plastically deformed zones have a slightly different orientation than the surrounding material, which creates contrast, e.g. bright against a dark background. It is evident from Fig. 7 that the plasticity introduced by indentation interfere with neighboring indents and the GB. This was also confirmed by the interacting strain fields between indents revealed by SPED analysis (Fig. 9). In light of the aforementioned experimental observations, it is suggested that the dislocations generated during nanoindentation close to the GBs will pile up and generate work hardening. After exceeding a critical stress level, dislocations can be transmitted into the adjacent grain (Figs. 7 and 9). The dislocation interaction with the GB depends on their type, GB character, grain orientations and loading conditions. The previously reported type of interactions includes dislocations absorbed in the GB, transmitted into the adjacent grain and/or absorbed dislocations re-emitted in the adjacent grain (Fig. 9) [25]. The hardness profile obtained from T4AC (Fig. 4) displays nearly constant hardness values across the GB, suggesting that dislocation pile-up at the GB has minor influence on hardness under loading conditions in the current work compared to interaction with precipitates. The elevated hardness obtained near the GB in T6AC and T6WQ is therefore suggested to instead be influenced primarily by the higher density and length of precipitates.

Figs. 7 and 9 also show that the plastic strain zones around the indents overlap. The effect of indent spacing on nanohardness is displayed in Fig. 3. It is observed that an indent spacing of 2 μm introduces a hardness increment (3(a)). The hardness peak reaches approximately 1.4 GPa, compared to 1.3 GPa for tests with 3 μm and 6 μm indent spacing. In contrast, hardness profiles presented in 3(b) and (c) are relatively comparable. In general, a minimum spacing of ten times the indentation depth is recommended. Possible deviation in hardness can be assessed considering normalized spacing defined as the ratio of indent spacing to the maximum depth [26]. For Al, a normalized spacing of minimum 10 should be sufficient to avoid deviation of hardness due to plasticity overlap between indents. In the current work, indent spacings of 2, 3 and 6 μm were used, corresponding to normalized spacings of 10, 15 and 30. The results indicate some hardness deviation for tests performed with an indent spacing of 2 μm, but no for spacings of 3 and 6 μm. The T6 specimens contain precipitates that result in higher strain hardening capability and consequently larger extension of the plastic zone. Therefore, the normalized spacing should preferably be greater 10. The high consistency in nanohardness in measurements above this normalized spacing, shows that the hardness increment highlighted in region III, is not a consequence of plasticity overlap between indents, but rather an effect of the higher precipitate density, giving rise to a higher hardening capability.

5. Conclusions

Nanoindentation and characterization with various electron microscopy techniques were performed across GBs and PFZs in Al–Mg–Si alloys with T4 and T6 temper conditions. The results reveal a lower hardness at the GB in the T6 sample due to the presence of PFZs, which is consistent with previous findings for this alloy. The hardness increases with increasing distance from the GB and reaches a peak value 2–3 μm from the GB. With further increasing distance from the GB, the hardness decreases and reaches comparable values to those found in the grain interior. The harder region adjacent to the GB was not present in the T4 sample. This finding is therefore attributed to an increased density and length of precipitates, consistent with the precipitate quantification from TEM analysis performed 2 and 100 μm from the GB. The discovery of this local hardness increase is reported for the first time and sheds light on inhomogeneities in the precipitate distribution and its effect on the mechanical properties of this alloy. This variation in precipitate distribution can act as a barrier for dislocation glide and probably accommodate plasticity in the softer PFZ.

CRediT authorship contribution statement

Anette B. Hagen: Writing – original draft, Writing – review & editing, Methodology, Investigation, Validation, Conceptualization, Visualization. **Sigurd Wenner:** Writing – review & editing, Methodology, Investigation, Visualization, Conceptualization. **Ruben Bjørge:** Writing – review & editing, Investigation, Validation. **Di Wan:** Writing – review & editing, Investigation. **Calin D. Marioara:** Conceptualization, Methodology. **Randi Holmestad:** Writing – review & editing, Resources, Conceptualization. **Inga G. Ringdalen:** Writing – review & editing, Resources, Methodology, Conceptualization, Supervision.

Declaration of competing interest

The authors declare that they have no known competing financial interests or personal relationships that could have appeared to influence the work reported in this paper.

Data availability

Data will be made available on request.

Acknowledgments

The authors acknowledge CASA - the Centre for Advanced Structural Analysis, funded by the Research Council of Norway [grant number 237885] and its industrial partners. The TEM and FIB work were performed on the NORTEM infrastructure at the TEM Gemini Centre at NTNU, Norway [grant number 197405] and NorFAB infrastructure at NTNU NanoLab, Norway [grant number 245963], respectively, both funded by the Research Council of Norway.

References

[1] Sigmund J. Andersen, Calin D. Marioara, Jesper Friis, Sigurd Wenner, Randi Holmestad, Precipitates in aluminium alloys, Adv. Phys.: X 3 (1) (2018) 1479984.
[2] G.A. Edwards, K. Stiller, G. Dunlop, M.J. Couper, The composition of fine-scale precipitates in Al-Mg-Si alloys, Mater. Sci. Forum 217 (1996) 713–718.
[3] K. Matsuda, Y. Sakaguchi, Y. Miyata, Y. Uetani, T. Sato, A. Kamio, S. Ikeno, Precipitation sequence of various kinds of metastable phases in Al-1.0 mass% Mg_2Si-0.4 mass% Si alloy, J. Mater. Sci. 35 (1) (2000) 179–189.
[4] S.J. Andersen, C.D. Marioara, A. Frøseth, R. Vissers, H.W. Zandbergen, Crystal structure of the orthorhombic U2-Al 4 Mg 4 Si 4 precipitate in the Al–Mg–Si alloy system and its relation to the β and β phases, Mater. Sci. Eng.: A 390 (1) (2005) 127–138.
[5] H.W. Zandbergen, S.J. Andersen, J. Jansen, Structure determination of Mg_5Si_6 particles in Al by dynamic electron diffraction studies, Science 277 (5330) (1997) 1221–1225.
[6] C.D. Marioara, H. Nordmark, S.J. Andersen, R. Holmestad, Post-β phases and their influence on microstructure and hardness in 6xxxAl-Mg-Si alloys, J. Mater. Sci. 41 (2) (2006) 471–478.
[7] Ketill O. Pedersen, Ida Westermann, Trond Furu, Tore Børvik, Odd Sture Hopperstad, Influence of microstructure on work-hardening and ductile fracture of aluminium alloys, Mater. Des. 70 (2015) 31–44.
[8] P.N.T. Unwin, G.W. Lorimer, R.B. Nicholson, The origin of the grain boundary precipitate free zone, Acta Metall. 17 (11) (1969) 1363–1377.
[9] Mikhail Khadyko, Calin Daniel Marioara, Inga Gudem Ringdalen, Stephane Dumoulin, Odd Sture Hopperstad, Deformation and strain localization in polycrystals with plastically heterogeneous grains, Int. J. Plast. 86 (2016) 128–150.
[10] Emil Christiansen, Calin Daniel Marioara, Knut Marthinsen, Odd Sture Hopperstad, Randi Holmestad, Lattice rotations in precipitate free zones in an Al-Mg-Si alloy, Mater. Charact. 144 (2018) 522–531.
[11] Bjørn Håkon Frodal, Emil Christiansen, Ole Runar Myhr, Odd Sture Hopperstad, The role of quench rate on the plastic flow and fracture of three aluminium alloys with different grain structure and texture, Internat. J. Engrg. Sci. 150 (2020) 103257.
[12] Tomo Ogura, Shoichi Hirosawa, Tatsuo Sato, Quantitative characterization of precipitate free zones in Al–Zn–Mg (–Ag) alloys by microchemical analysis and nanoindentation measurement, Sci. Technol. Adv. Mater. 5 (4) (2004) 491–496.
[13] V. Radmilovic, C. Taylor, Zonghoon Lee, A. Tolley, D. Mitlin, U. Dahmen, Nanoindentation properties and the microstructure of grain boundary precipitate-free zones (PFZs) in an AlCuSiGe alloy, Phil. Mag. 87 (26) (2007) 3905–3919.
[14] Takuya Hashimoto, Ken-ichi Ikeda, Seiji Miura, Relationship between mechanical properties and age-hardening behavior around grain boundaries of Al-Mg-Si alloy, in: MATEC Web of Conferences, Vol. 326, EDP Sciences, 2020.
[15] Takuya Hashimoto, Ken-ichi Ikeda, Seiji Miura, Effect of grain boundary characters on precipitation behavior and local deformation behavior in Al-Mg-Si alloy, J. Japan Inst. Metals Mater. 85 (1) (2021) 7–16.
[16] Mary F. Doerner, William D. Nix, A method for interpreting the data from depth-sensing indentation instruments, J. Mater. Res. 1 (4) (1986) 601–609.
[17] Stefan Zaefferer, Nahid-Nora Elhami, Theory and application of electron channelling contrast imaging under controlled diffraction conditions, Acta Mater. 75 (2014) 20–50.
[18] Sigmund J. Andersen, Quantification of the Mg 2 Si β and β phases in AlMgSi alloys by transmission electron microscopy, Metall. Mater. Trans. A 26 (8) (1995) 1931–1937.
[19] P.M. Kelly, A. Jostsons, R.G. Blake, J.G. Napier, The determination of foil thickness by scanning transmission electron microscopy, Phys. Status Solidi (A) 31 (2) (1975) 771–780, http://dx.doi.org/10.1002/pssa.2210310251.
[20] The crystal structure of the β'' phase in Al-Mg-Si alloys, Acta Mater. 46 (9) (1998) 3283–3298.
[21] Calin D. Marioara, Adrian Lervik, Julie Grønvold, Otto Lunder, Sigurd Wenner, Trond Furu, Randi Holmestad, The correlation between intergranular corrosion resistance and copper content in the precipitate microstructure in an AA6005A alloy, Metall. Mater. Trans. A 49 (10) (2018) 5146–5156.
[22] Sigurd Wenner, Calin Daniel Marioara, Sigmund Jarle Andersen, Randi Holmestad, Effect of room temperature storage time on precipitation in Al–Mg–Si (–Cu) alloys with different Mg/Si ratios, Int. J. Mater. Res. 103 (8) (2012) 948–954.
[23] Zi Yang, John Banhart, Natural and artificial ageing in aluminium alloys – the role of excess vacancies, Acta Mater. 215 (2021) 117014.
[24] R.W. Balluffi, R.F. Mehl, Grain boundary diffusion mechanisms in metals, Metall. Mater. Trans. B 13 (1982) 527–553.
[25] Farhan Javaid, Habib Pouriayevali, Karsten Durst, Dislocation–grain boundary interactions: recent advances on the underlying mechanisms studied via nanoindentation testing, J. Mater. Res. (2021) 1–13.
[26] P. Sudharshan Phani, W.C. Oliver, A critical assessment of the effect of indentation spacing on the measurement of hardness and modulus using instrumented indentation testing, Mater. Des. 164 (2019) 107563.